ORIGINAL ARTICLE

Journal of Anatomy ANATOMICAL SOCIETY WILEY

How compactness affects long bone resistance to compression—An investigation into the rhinoceros humerus

Cyril Etienne[1] | Jérémie Viot[1] | Peter J. Watson[2,3] | Michael J. Fagan[2] |
Alexandra Houssaye[1]

[1]Mécanismes Adaptatifs et évolution
(MECADEV), UMR 7179, MNHN, CNRS,
Paris, France

[2]Biomedical Engineering Research Group,
School of Engineering, University of Hull,
Hull, UK

[3]Institute of Medical and Biological
Engineering, School of Mechanical
Engineering, University of Leeds, Leeds,
UK

Correspondence
Alexandra Houssaye, Mécanismes
Adaptatifs et évolution (MECADEV), UMR
7179, MNHN, CNRS, Paris, France.
Email: houssaye@mnhn.fr

Funding information
ERC-2016-STG-715300

Abstract

The functional signal of bone internal structure has been widely studied. Isolated form-function relationships have often been assumed from the observation of presumed morphofunctional relationships, but have never been truly tested. Indeed, distinct bone microanatomical feature co-evolve in response to various constraints that are difficult to detangle. This study tested for the first time the impact of various microanatomical parameters taken one by one, plus some in pairs, on bone strength under compression using biomechanical modelling. We carried out finite element analyses on humerus models, obtained from a white rhinoceros, with different heterogeneous internal structures, and analysed the magnitude and distribution of von Mises stresses. These tests validated earlier hypotheses of form-function relationships about the greater resistance to compression provided by the thickening of the cortex and the filling of the medullary area by trabecular bone and highlighted the stronger impact of increasing trabecular bone compactness than of avoiding an open medullary cavity. By making it possible to estimate the relative impact of each parameter and of combinations of microanatomical features, they also showed the more limited impact of the trabecular bone compactness in the epiphyses to resist compression, and the fact that microanatomical changes of opposite but of similar amplitude impact can compensate each other, but that the impact of the sum of two negative microanatomical changes far exceeds the sum of the impacts of each of the two changes taken separately. These results contribute to a better understanding of bone adaptation and form-function relationships so that they later can be used with confidence for palaeobiological inferences on fossil specimens, contributing to a better understanding of skeletal evolution during the evolutionary history of vertebrates. They also highlight the potential of taking internal structure into account in the bone biomechanical analyses. In addition, they can be used in bioinspiration to design resistant structures subjected to compression.

KEYWORDS
biomechanical modelling, bone adaptation, compactness, compression

1 | INTRODUCTION

The inner structure of bone, like any biological structure, answers to various different constraints, including historical, structural, developmental, and also functional (Gould, 2006; Seilacher, 1970). The link between bone inner structure and functional requirements has been highlighted in various skeletal elements and various taxa (Canoville & Laurin, 2010; Dumont et al., 2013; Houssaye, Martin Sander, & Klein, 2016; Kivell et al., 2011; Mielke et al., 2018; Quemeneur et al., 2013) and the relationship between bone density and trabecular architecture (density/orientation) and functional requirements has been widely investigated in humans (DeMars et al., 2021; Querol et al., 2006; Saers et al., 2016; Turner, 1998). Many inferences have thus been made about the relationships between bone inner structure and the functional constraints experienced by bones. These hypothetical form-function relationships have been largely used to propose paleobiological inferences based on fossil bone microanatomy (Canoville et al., 2021; Cerda et al., 2015; Dunmore et al., 2020; Hayashi et al., 2013; Klein et al., 2019; Ksepka et al., 2015; Straehl et al., 2013). However, in nature, various functional constraints are mixed and it is difficult to precisely determine how one specific anatomical feature affects one function, which limits the strength of the hypotheses about the relationships between microanatomical features and function. The focus on one single feature and on one single function is nevertheless possible thanks to biomechanical modelling.

The objective of this study is to examine bone microanatomical features associated with strength under compressive load in the skeleton. To do so, the study focuses on one limb bone of a heavy mammal since these taxa have long bones that are well adapted to support a heavy weight. Furthermore, in order to enable the optimum investigation, and application of the results to most other quadrupedal mammals, we selected a heavy mammal whose skeleton is not too strongly adapted to support a heavy weight so that gallop is still possible (unlike in elephants; Ren et al., 2010): the rhinoceros. The hippopotamus could also have been chosen but it is semiaquatic, so that its skeletal inner structure is also adapted to aquatic locomotion (Houssaye et al., 2021); therefore we preferred the "simplicity" of a terrestrial rhinoceros. We thus selected the white rhinoceros *Ceratotherium simum*, which weighs an average of 2300 kg (Dinerstein, 2011). Stylopod bones are the ones whose microanatomy is the most investigated, so analysing a stylopod bone would be the most beneficial for comparative analyses. Moreover, all the weight of the leg passes through them (whereas it is divided between the radius and ulna, tibia and fibula for the zeugopod). The forelimb in rhinos, as in most non-primate quadrupedal mammals, is more involved in body support whereas the hindlimb is more involved in propulsion (Dutto et al., 2006; Lessertisseur & Saban, 1967; Mallet et al., 2019). We thus investigated the humerus of *Ceratotherium*.

Long bones of heavy amniotes are known to possess a relatively thick cortex and a medullary area (mostly if not entirely) filled by trabecular bone (Houssaye et al., 2016c 2021; Nganvongpanit

et al., 2017; Lefebvre et al., 2023; Wall, 1983). We therefore expect to see that both a thickening of the cortex and the filling of the medullary area by trabecular bone provide greater resistance to compression. We also wonder to what extent trabecular bone compactness, that is, the bone volume fraction (BVF) (volume of the osseous tissue over the total volume), has an impact on bone strength under compressive load. To investigate this, finite element analyses associated with compressive load are performed on humeri with different heterogeneous inner structures. These models are based on a humerus whose original microstructure is simplified and modified in order to individually test the biomechanical impact of several microanatomical parameters. We thus investigate the impact of hollowing out a medullary cavity, changing cortical thickness, and of changing the density of trabecular bone in the different regions of a humerus. We also analyze the impact of pairs of parameters to see if they could compensate for each other, and to estimate the impact of the two parameters relative to the sum of the individual impacts of each of them. These results offer, for the first time, the opportunity to test isolated form-function relationships that are generally only assumed in micraoanatomical analyses, and to compare their relative strengths. It will permit strengthening of the characterization of the microanatomy-function relationships, and thereby improve our understanding of bone adaptation. This will in turn also lead to more accurate paleobiological inferences that can be made on fossil taxa based on their long bone microanatomical features.

2 | MATERIALS AND METHODS

2.1 | Design of the models

The humerus selected was that of the *Ceratotherium simum* specimen NMB 8029 (Naturhistorisches Museum Basel, Switzerland), which was an adult (based on the complete fusion of the epiphyses) male specimen caught in the wild (Uganda). The bone was entirely scanned using microtomography with a GE Phoenix|X-ray v|tome|xs 240 on the AST-RX platform at the Muséum National d'Histoire Naturelle, Paris (UMS 2700), at a voxel size of 103.6 μm, which enabled us to visualize all individual trabeculae, with reconstructions performed using DATOX/RES software (Phoenix Datos|x). Bone tissue was entirely segmented from bone marrow and fixation material. Segmentation was performed using the Trainable Weka segmentation plugin of imaging processing software ImageJ (Schindelin et al., 2012), designed from the Waikato Environment for Knowledge Analysis (Arganda-Carreras et al., 2017). This machine learning technique takes as input a few of the CT-scan slices (illustrating a diversity of regions with different contrasts between bony and non-bony areas) that were segmented manually, and then segments the entire CT-scan raw data based on the pre-segmented samples. The segmentation was then checked and corrected in VGStudio MAX (v2.2.7, Volume Graphics GmBH, 2016). The segmented complete bone was further divided into numerous volumes of interest (VOI) within Dragonfly (Object

Research Systems, 2021) in order to make compactness cartographies with the BoneAnalysis plugin. This generates small spherical VOIs that are distributed over a 3D grid across the whole bone. The spacing of the VOIs was defined as the sum of the average trabecular thickness and trabecular spacing values. These were obtained based on the isolation of trabecular bone from cortical bone and a thin layer of compact bone at the periphery of the epiphyses by manual segmentation (see Houssaye et al., 2018) and the BoneAnalysis plugin. The radius of each VOI was defined as twice the distance of the VOI spacing; we thus obtained a spacing of 1.2 mm and a radius of 2.4 mm for the VOIs, spread all over the bone in a regular 3D grid pattern.

BVF was calculated for each VOI, defining its compactness (i.e., volume of bone tissue over total volume of the VOI; between 0 [no bone voxel in the VOI] and 1 [only bone voxels in the VOI]). It was then possible to export the cartography from Dragonfly as an image stack, with one voxel per VOI (and thus a resolution of 1.2 mm per voxel), and import it to Avizo 9.0 (VSG, Burlington, MA, USA). We could then determine compactness intervals based on the compactness histogram obtained for the whole bone (Figure S3). The aim was to establish several compactness intervals to design different materials (with distinct material properties) to be used in FEA, as compactness is by far the main determinant of trabecular bone stiffness (Maquer et al., 2015; Stauber et al., 2006). As a compromise between time and scientific significance, we selected five intervals and designed accordingly five materials (to be made up by all VOIs showing the corresponding compactness values) for the trabecular bone: M1) from 0.0001 to 0.2999; M2) from 0.3 to 0.3999; M3) from 0.4 to 0.4999; M4) from 0.5 to 0.5999; M5) from 0.6 to the maximal values that were around 0.85. Since most of the compactness values are between 0.3 and 0.6, the intervals are smaller between these values. Trabecular bone was then separated into the five materials depending on VOI compactness (i.e., we defined territories incorporating VOIs in the appropriate compactness range for each material) using the threshold function, and a compact bone material was further added (M6), determined not from bone compactness but directly from the manual segmentation mentioned above. This segmentation was very close to the biology but inevitably several contours between materials were very irregular, or thin (i.e., only one or two voxels), which would have prevented the making of a suitable 3D mesh (since some tetrahedra would have been very thin and elongated) to extract from Avizo to FEA software ANSYS (v. 2020 R1, ANSYS Inc., 2020). As a consequence, some smoothing was necessary, through the Smooth labels, Shrink/Growth Volume and/or Interpolate functions in Avizo to reduce the irregularities of the compactness patches (i.e., protrusions or troughs of 2 or 3 voxels) and remove the islands (i.e., patches of a few [<10] isolated voxels). This resulted in most of the compact bone material in the periphery of the epiphyses, where it is usually very thin, being included in the closest trabecular material instead. A 3D Model made from this slightly simplified segmentation still showed some irregular contours and some very thin patches (one or two voxels wide), preventing Avizo from making a 3D mesh. We thus performed a further

smoothing step by simplifying the shape of the compactness patches to sharply contoured patches and simplified shapes. The aim was to obtain a structure representing the distribution of the compactness patches within the humerus, but simplifying their shape sufficiently to ensure that it could be transformed into a 3D mesh, either by automatic smoothing with the Smooth labels function or by manually drawing over the region borders (using the interpolate function to avoid having to draw on each slice). 3DM1 (Figure 1b,h) was made from this simplified segmentation. All the following models (Table 1) were made from this reference model:

- 3DM2, to test the effect of a thicker cortical bone (changing only the inner structure, not the morphology). The material corresponding to the cortical bone (M6) was enlarged towards the core of the bone, by incorporating voxels of the trabecular material with the function Growth-Volume used five times (volume expanded by five voxels [i.e., 6 mm] in all directions) and subsequently removing the part outside the original external profile of the bone (Figure 1c,i) so that the bone morphology is not altered and cross sectional area not modified;

- 3DM3, to test the effect of a thinner cortical bone. The M6 material was shrunk using the Shrink – Volume function five times. Again, only the inner structure was changed, thus only the inner border of the cortical material was shrunk. The removed voxels were added to a separate material, with the same material properties as the M4 trabecular material (compactness between 0.5–0.6; Figure 1d,j), since it corresponds to the average trabecular compactness of this bone.

- 3DM4, to test the effect of an open medullary cavity. The medullary cavity was designed from the area of least compactness in the centre of the humeral shaft (which corresponded to a cylindrical shape belonging mainly to M1) and was extended so that it had similar shape and delimitations as that of an American bison (*Bos bison*), based on longitudinal sections available at the laboratory. This taxon was chosen since it is a rather heavy animal (360 to 544 kg for females, 460 to 998 kg for males [Castelló, 2016]), but still has an open medullary cavity in its long bones. Finally, the medullary cavity is about the shape of a tube with rounded extremities extending mostly in the diaphysis (from the end of the medial curve which leads to the convexity of the lesser tubercle to just above the olecranon fossa), where trabecular bone is reduced (Figure 1e,k);

- 3DM5, to test the effect of changes of compactness of trabecular bone in the epiphyses only. All the voxels in the epiphyses, of all materials except cortical bone and thin layer of compact bone at the periphery (M6), were moved to new, separate materials. This firstly required the identification of the boundary between the epiphyses and metaphyses, which was ambiguous based on our specimen. This was facilitated by the observation of scans of a subadult specimen of the same species, whose epiphyses were not yet perfectly fused. A material corresponding to each epiphysis was then generated in a new Avizo label field, by drawing directly on some slices and interpolating between them, imitating
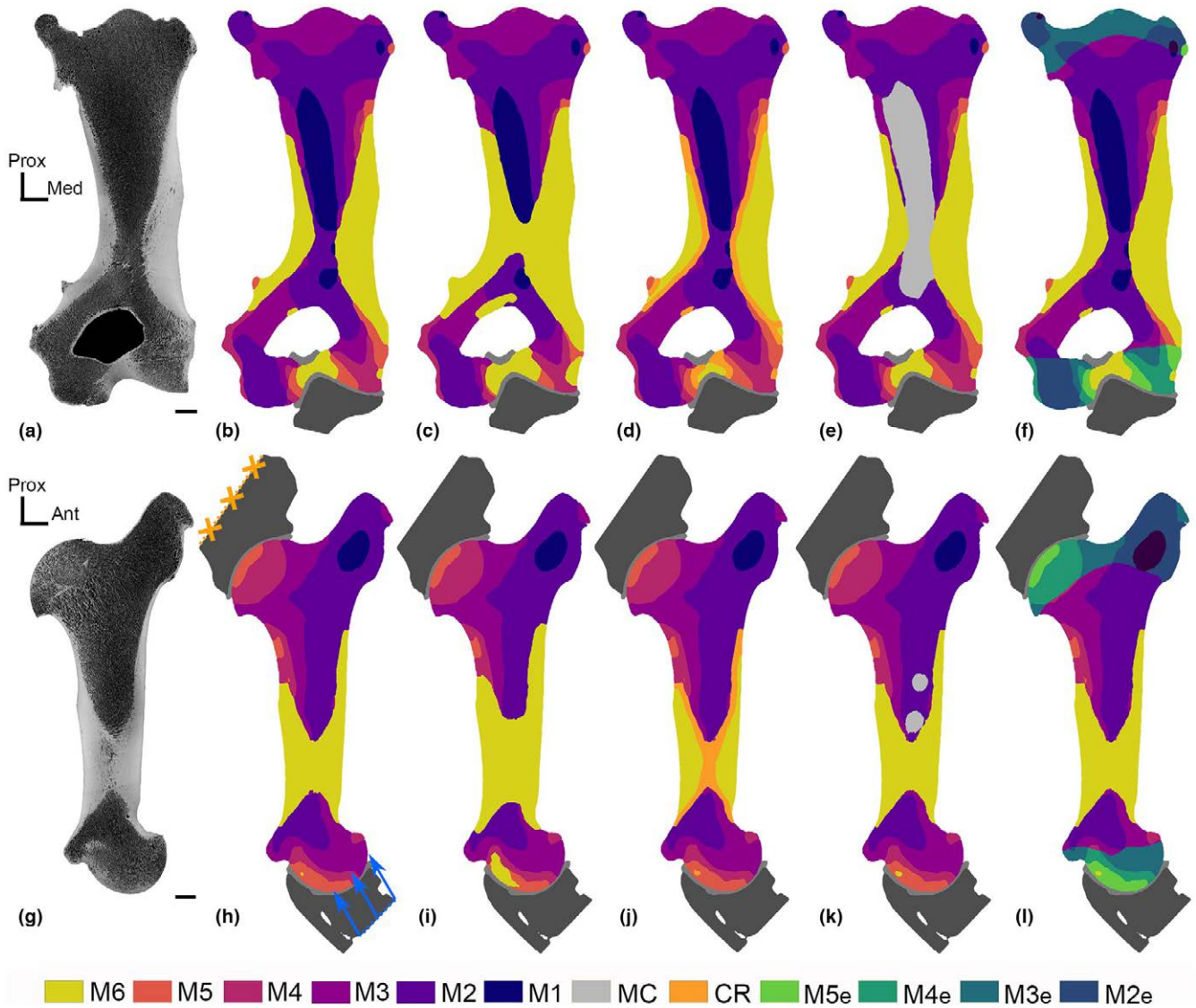
FIGURE 1 Coronal (a; top) and sagittal (g; bottom) sections and associated views of the models 3DM1 (b, h), 3DM2 (c, i), 3DM3 (d, j), 3DM4 (e, k), and 3DM5 (f, l) with different colors indicating different materials. MC: Medullary cavity; CR: Cortex replacement; e: Epiphysis. Scale bar equals 2 cm. In h the orange crosses indicate where the bone is constrained, and the blue arrows indicate where the force is applied. The light-grey materials on the surface of the joint between the humerus and the dark-grey materials for the partial bones (MS for the scapula proximally and MRU for the radius-ulna distally) correspond to the cartilaginous materials (MCP and MCD, respectively).

the position of the epiphyseal line observed on the subadult individual. Intersections between the epiphyseal materials and the M1-M5 trabecular materials allowed the separation of the M1e-M5e materials in the epiphyses (Figure 1f,l).

Moreover, beyond analysing the relative impact of each parameter independently, we also aimed to analyse the impact of the combined effect of two parameters. For that, we built two additional models:

- Combo1, combining a thicker cortex and a medullary cavity, to evaluate if the former, a positive effect, compensates the latter, a negative one; we used the same method as for both 3DM2 and 3DM4.

- Combo2, combining a thinner cortex and a medullary cavity, to estimate the relative impact of cumulating these two negative factors; we used the same method as for both 3DM3 and 3DM4.

In order to have a realistic direction and distribution of the forces at the joint contact area, part of the adjacent bones and thus of the joints were also included in the model. The scapula, radius and ulna fragments, as well as the cartilage, would thus diffuse the stresses before they reach the humerus and avoid artefactually high stresses at the nodes where the forces and constraints are applied. To articulate the scapula and radius-ulna with the humerus in the correct anatomical position, 3D models of each bone were imported into Blender (v2.81, Blender Foundation, 2018), and aligned to be in an anatomical position with the humerus. The space between the

TABLE 1 List of the models analyzed and compactness of the associated materials.

3D model		Description	Materials' compactness						Von Mises stress (MPa)	
			M1	M2	M3	M4	M5	M6	95th per.	99th per.
3DM1	3DM1A	Simplified segmentation with changes in compactness of trabecular & cortical bone	0.25	0.35	0.45	0.55	0.65	1	30.1	48.2
	3DM1B		0.55	0.55	0.55	0.55	0.55	1	27.8	41.8
	3DM1C		0.45	0.45	0.45	0.45	0.45	1	28.2	44.5
	3DM1D		0.35	0.35	0.35	0.35	0.35	1	28.6	47.8
	3DM1E		0.45	0.45	0.45	0.45	0.45	0.45	25.5	35.2
	3DM1F		0.55	0.55	0.55	0.55	0.55	0.55	25.5	35.2
3DM2		Thicker cortex	0.25	0.35	0.45	0.55	0.65	1	28.7	43.5
3DM3		Thinner cortex	0.25	0.35	0.45	0.55	0.65	1	27.9	47.3
3DM4		Medullary cavity	0.25	0.35	0.45	0.55	0.65	1	30.4	50.0
3DM5	3DM5A	Changes in the trabecular compactness of the materials in the epiphyses and in the diaphysis and metaphysis separately	0.25 epy: 0.15	0.35 epy: 0.25	0.45 epy: 0.35	0.55 epy: 0.45	0.65 epy: 0.55	1	29.8	48.4
	3DM5B		0.25 epy: 0.35	0.35 epy: 0.45	0.45 epy: 0.55	0.55 epy: 0.65	0.65 epy: 0.75	1	29.0	46.5
	3DM5C		0.15 epy: 0.25	0.25 epy: 0.35	0.35 epy: 0.45	0.45 epy: 0.55	0.55 epy: 0.65	1	29.9	50.7
	3DM5D		0.35 epy: 0.25	0.45 epy: 0.35	0.55 epy: 0.45	0.65 epy: 0.55	0.75 epy: 0.65	1	28.9	45.0
Combo1		Thicker cortex & medullary cavity	0.25	0.35	0.45	0.55	0.65	1	28.7	44.7
Combo2		Thinner cortex & medullary cavity	0.25	0.35	0.45	0.55	0.65	1	30.7	54.1
Combo3		Thinner cortex (3DM3) with increased compactness of trabecular bone	0.35	0.45	0.55	0.65	0.75	1	27.4	44.2
Combo4		Medullary cavity (3DM4) with increased compactness of trabecular bone	0.35	0.45	0.55	0.65	0.75	1	29.6	47.1

Abbreviations: Epy: Epiphyses. Per: Percentile values of the Von Mises Stress calculated for the various models.

humerus and the different bones determined the thickness of the future cartilage material, thus a typical distance of 2.5 mm was defined between the scapula and humerus, following Mancini et al. (2019). The articular surface of the radius-ulna for the humerus wrapped almost entirely around the humeral trochlea making the definition of a homogeneous cartilage thickness over the articular surface more difficult, but the average thickness is similar to that at the scapula. The 3D models of the radius-ulna and scapula were then imported to Avizo, and converted into labels using the Scan Surface to Volume function. A cartilage material was generated to link the bones. At this point, voxel size was divided by two (i.e., each voxel was separated into 8 voxels) and the labels were smoothed again, to increase the resolution, which made the 3D mesh generation easier. The final Avizo labels consisted of the various humeral materials, the cartilage (MCP and MCD for the cartilage located proximally and distally to the humerus, linking it to the scapula and radius-ulna respectively), and the cut-out parts of the scapula (MS) and radius-ulna (MRU).

Once the materials for all the desired models were generated in Avizo, they were thus transformed into a single 3D volumetric mesh, filled by 10-node second order tetrahedra, to be imported into ANSYS for FEA. The first step was to generate a hollow 3D surface from the materials, from which the filled 3D mesh will be generated. The surface had to meet several quality criteria. Notably, the surfaces must be closed, the triangles must not intersect, and the expected aspect ratios of all the 3D mesh's tetrahedra should be below 20 (i.e, the triangles should be reasonably regular and not too elongated). The surface was first generated with the Generate surface function, decimated down to 500,000 faces (as this, empirically, gives a FE model close to the limit of our computation power [192 GB of RAM]), and then remeshed to increase mesh regularity. In two cases (3DM2 and 3DM3), before the remesh, the surfaces were smoothed using the Smooth Surface function. The remeshed surfaces were corrected in the Surface Editor so that each of the parameters reached the threshold value required; thus, ANSYS could solve the model with no warnings. This was done automatically with the functions PrepareTetraGen, fixIntersection, fixDihedralAngle, and fixTetraQuality, which generally corrected a large proportion of the errors. A few remaining triangles were corrected using Avizo's manual correction tools. The 3D volumetric mesh was then generated using the Generate Tetra Grid function in Avizo, filling the volume with tetrahedra (similar to those of the mesh surface). The various 3D models for which 3D meshes could be generated correspond to seven different arrangements of the different materials (3DM1-5, Combo1-2; Figure 1).

2.2 | Material properties

Once the 3D meshes were generated for each model, including materials of varying compactness for the humerus (Table 1), it was necessary to determine the mechanical properties of each material, in particular the Young's modulus of elasticity (reflecting the stiffness of the material). The Young's modulus of the trabecular bone depends primarily on its compactness (Currey, 2006). In order to determine that relationship for this particular bone, 14 cubic regions of the bone (13 trabecular, 1 cortical) were virtually sampled from the segmented CT-scan and tested for their Young's modulus, using a custom ANSYS routine (see Supplementary data SD1 for details). The Young's modulus of each of these regions was correlated to its compactness with a second-degree polynomial equation, that was found to fit extremely well to the data ($R^2 = 0.997$). The resulting equation was $E = 18,828 \times C^2 - 1731 \times C + 124.35$, with $E =$ Young's modulus in MPa and $C =$ compactness. Using this equation, Young's modulus was then attributed to the different materials of the different models based on their averaged compactness.

For all models, the cortical bone was considered to have a compactness of 1, resulting in a Young's modulus of 17,221 MPa. The scapula, radius and ulna have a compactness set at 0.55 (corresponding to a Young's modulus of 4867 MPa), as the extremities of the bones are expected to be made up primarily of dense trabecular bone (as for the humerus). In the 3DM1 model, since the idea was to compare theoretical models, arbitrary compactnesses based on the histogram (Figure S3) were set at 0.25, 0.35, 0.45, 0.55 and 0.65 respectively for M1 to M5, corresponding to Young's moduli of 868, 1825, 3158, 4867 and 6954 MPa, respectively. For tests (on 3DM1 and 3DM5) implying changes in the compactness of the trabecular bone, when it came to increasing the compactness, we added 0.10 and, similarly, we removed 0.10 to reduce the compactness.

In order to test the impact of changes in the compactness of the trabecular bone and cortex, we used five versions of the 3DM1 model (Table 1): (1) 3DM1A, the reference model, with materials having the compactness values cited above; (2–4) 3DM1B-D with all the trabecular bone being homogeneous, with a single compactness value, equal to: 0.35 (3DM1B), 0.45 (3DM1C), and 0.55 (3DM1D), respectively. Moreover, (5) 3DM1E-F were made with homogeneous properties for all humeral materials (even compact bone so that it only consisted in trabecular bone), with a compactness of 0.45 (3DM1E) and 0.55 (3DM1F), respectively.

For 3DM2 (thicker cortex), 3DM3 (thinner cortex), and 3DM4 (with an open medullary cavity), the compactness values of the materials are the same as in 3DM1A. For 3DM3, the trabecular bone obtained by reducing the thickness of the cortex was essentially in contact with M3 and M4 but also, though to a lesser extent, to M5. Its compactness was estimated as 0.55, an intermediate value between those of these three materials. For 3DM4, rather than delete the voxels (elements) in the medullary cavity, they were simply defined with a Young's modulus of 0.001 MPa. This meant that they contributed nothing to the model stiffness, but kept the element numbers the same simplifying post-processing.

For 3DM5, we used 4 versions to test the impact of varying the trabecular compactness of the materials in the epiphyses and in the diaphysis and metaphyses, separately: 1) 3DM5A, where the compactness of the trabecular materials of the epiphyses are reduced, as described above, by −0.10, to compare with 3DM1A); 3DM5B, where the compactness of the trabecular materials of the epiphyses are increased, as described above, by +0.10; 3DM5C-D, where the

compactness of the trabecular materials belonging to the diaphysis and metaphyses are decreased (3DM5C) and increased (3DM5D) as described above.

For Combo1 the compactness values of the materials are the same as in 3DM4, while compactness values of Combo2 are the same as in 3DM3 and 3DM4. In addition, we analyzed two additional combinations:

- Combo3, combining a thinner cortex with an increased compactness of trabecular bone, to see how the positive effect of the latter parameter compensates the negative effect of the former. For that we used 3DM3 but increased the compactness of each trabecular material by 0.10.
- Combo4, combining a medullary cavity with an increased compactness of trabecular bone, to see how the positive effect of the latter parameter compensates the negative effect of the former. For that we used 3DM4 but increased the compactness of each trabecular material by 0.10.

The second important mechanical parameter is Poisson's ratio. It is the negative ratio of the transverse strain induced by a given axial strain, describing how a material deforms perpendicular to a given direction when the material is loaded in that direction. For all materials corresponding to bone, cortical or trabecular, it varies little, and hence is fixed at 0.3 (Currey, 2006). It was defined as 0.4 for cartilage (Laasanen et al., 2003).

2.3 | Loading conditions

We aimed at testing the impact of the various microanatomical features on the resistance to compressive loading on the bones in the skeleton. This loading applied aimed to provide a realistic representation of the true physiological loading, albeit with some simplifications that are inevitable with such biomechanical modelling. Since this study methodology is designed on the relative comparison between the separate models, the loading was kept consistent between all models. A musculoskeletal model of the forelimb of *C. simum* standing at rest had previously been performed using the OpenSim software (Etienne et al., 2024), we used the resultant compressive force of 15,638 N at the elbow in order to remain close to the real compressive load even in this simplified modelling comparative approach (this value was corrected to 14,835 N in the final OpenSim model, but, again, this change does not impact our relative comparisons). To adapt to the reference frame used in the FE analysis (with the X axis in the medio-lateral plane, the Y axis in the proximo-distal plane, and the Z axis in the cranio-caudal plane of the bone), we applied three force components to the nodes of the surface of the truncated part of the radius: −4633 N in the X axis, 11,448 N in the Y axis and 9593 N in the Z axis. The model was constrained at the scapula, with all nodes of the truncated part being fixed in all degrees of freedom. We thus only considered compression from the contact forces and not the muscular tensions that also

apply on the bone. All materials were part of the same mesh (i.e. connected at each node) so that the direction and distribution of the contact forces were modelled as accurately as possible, without the need for interaction constraints.

Once each model was run, we analyzed the results by looking at the distribution of Von Mises stresses, which correspond to a scalar function of the three principal stresses, and can be used to provide a general indication of the level of stress at a point, and as a predictor of bone failure (Rayfield, 2007). The closer the Von Mises stress at a given point is to the local strength value of the bone, the closer the structure is to failure at that point. Von Mises stresses were preferred to normal stresses to account for the various stresses generated by the compressive force, and not just compressive stresses. Indeed, the complex shape of the bone implies that bending will occur and some areas will be loaded in tension, and this must be taken into account to appreciate the impact on fracture risk.

Stresses were mapped on and within the humerus for each node. Von Mises (VM) color scales in most models are set to that of the 3DM1A reference model in order to visualize relative changes (as illustrated in Figure 2); however, they have been adapted for some models to better visualize regions of maximum values (i.e., in instances when the original color scale hampered the ability to clearly identify regions with the maximum values).

In order to compare distribution and maximal (magnitude) values of the Von Mises stresses between the various models, we made frequency graphs (Figures 4 and 8) and calculated the 95th and 99th percentile values (Table 1), following Walmsley et al. (2013), as the pure maximum stress value is often artefactual.

3 | RESULTS

3.1 | General distribution of the stress

Overall, Von Mises stresses on the bone outer surface are maximal: caudally in the proximal part of the diaphysis, below the humeral head and medio-cranially in the middle of the proximal part of the diaphysis above the teres major tuberosity (Figure 2a; S4–S8). The longitudinal sections show that Von Mises stresses are higher in the cortical area but also above the humeral head and in its distal half, whereas they are minimal in the medullary area, in the lesser and greater tubercles and in the distal epiphysis (Figure 3; S9,S10). Stresses are generally higher in parts of the model with higher stiffness (linked to the Young's modulus but also to the cross-section and relative position) as expected, and the maximal magnitudes are restricted to the outer surface of the bone, the cortex being structurally stiffer than trabecular bone, particularly under bending and torsion. The 95th and 99th percentile values calculated for each model (Table 1) are strongly correlated ($r = 0.93$).

This stress distribution shows that the stresses are the highest below the humeral head, in the concavity which is naturally subject to stress concentration because of bending. It is also more subject to high stress in the proximal half of the diaphysis. We cannot prevent
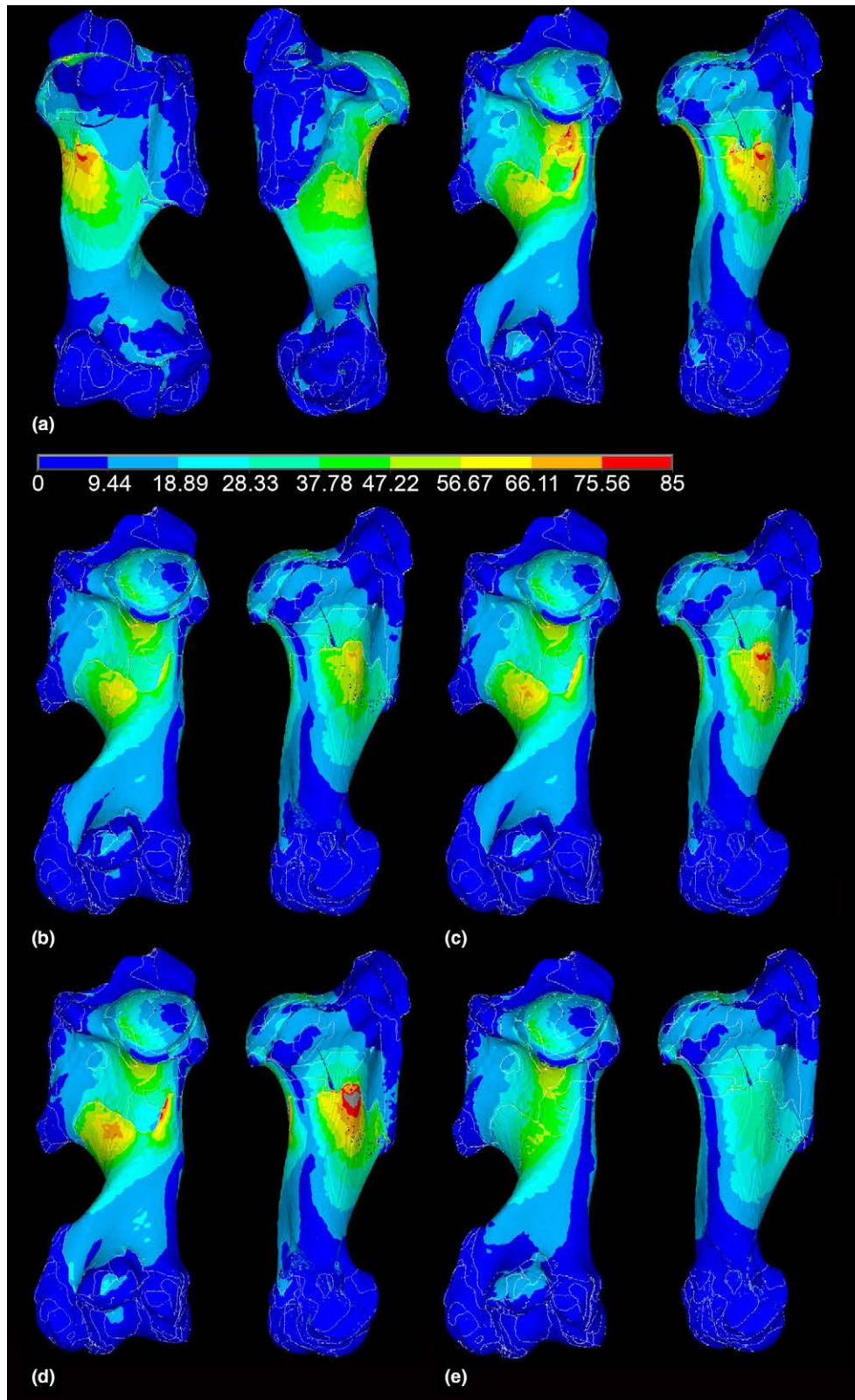
FIGURE 2 Cartographies of the Von Mises Stress distribution in (a) 3DM1A (base model), (b) 3DM1B (homogeneous trabecular bone with high compactness), (c) 3DM1C (homogeneous trabecular bone with average compactness), (d) 3DM1D (homogeneous trabecular bone with low compactness), (e) 3DM1E (homogeneous trabecular bone and cortex with average compactness), in (from left to right) cranial, lateral, caudal, and medial views for 3DM1A, and in (from left to right) caudal and medial views for the other models. VM scale in MPa. Grey areas correspond to stress magnitudes beyond red.
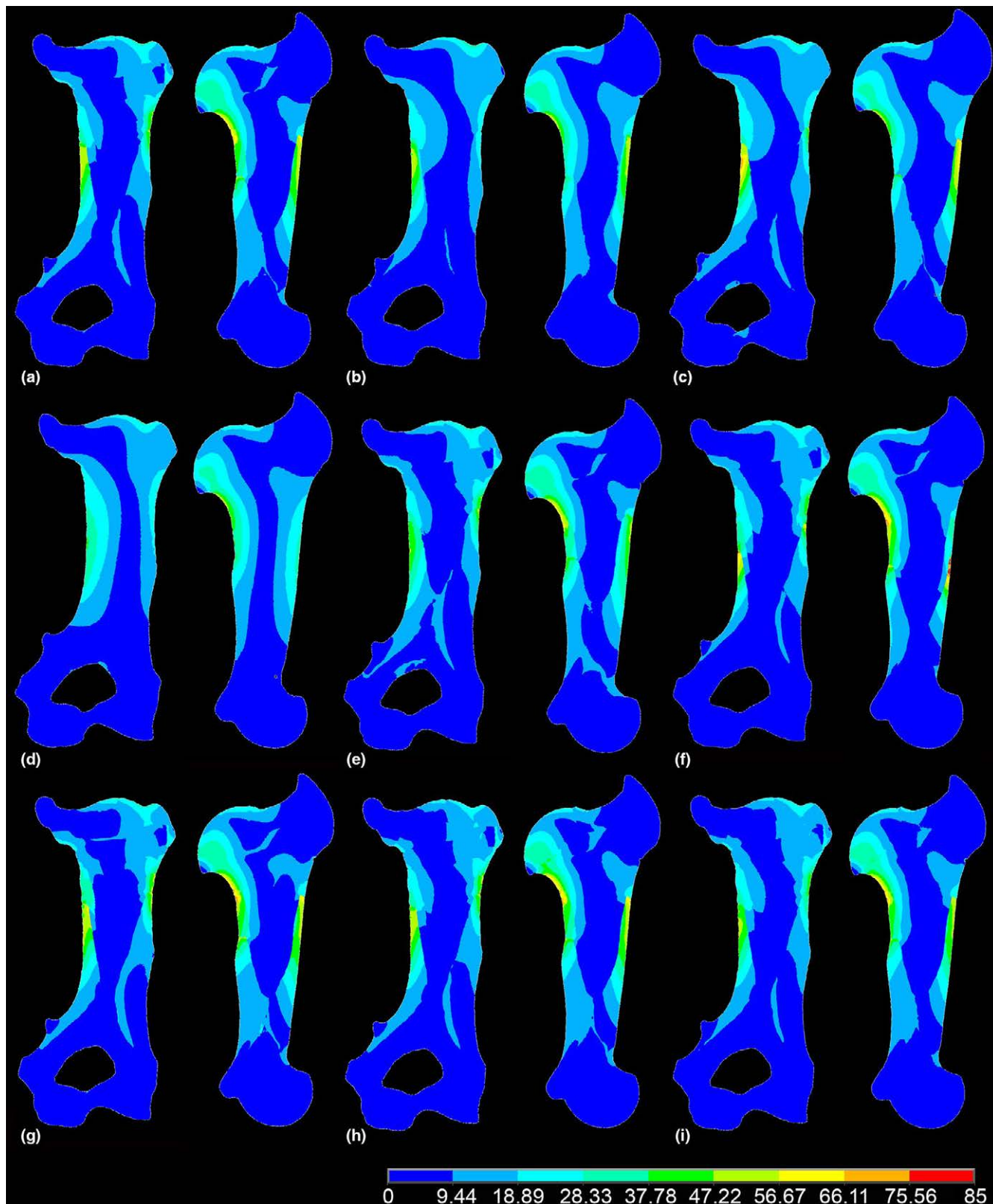
FIGURE 3 2D longitudinal sections in coronal (left) and sagittal (right) views illustrating the Von Mises stress distribution inside the bone. (a) 3DM1A (base model), (b) 3DM1B (homogeneous trabecular bone with high compactness), (c) 3DM1D (homogeneous trabecular bone with low compactness), (d) 3DM1E (homogeneous trabecular bone and cortex with average compactness), (e) 3DM2 (thicker cortex), (f) 3DM3 (thinner cortex), (g) 3DM4 (open medullary cavity), (h) 3DM5A (decreased compactness in the epiphyses), and (i) 3DM5D (increased compactness in the diaphysis and metaphyses). VM stress color scale in MPa.
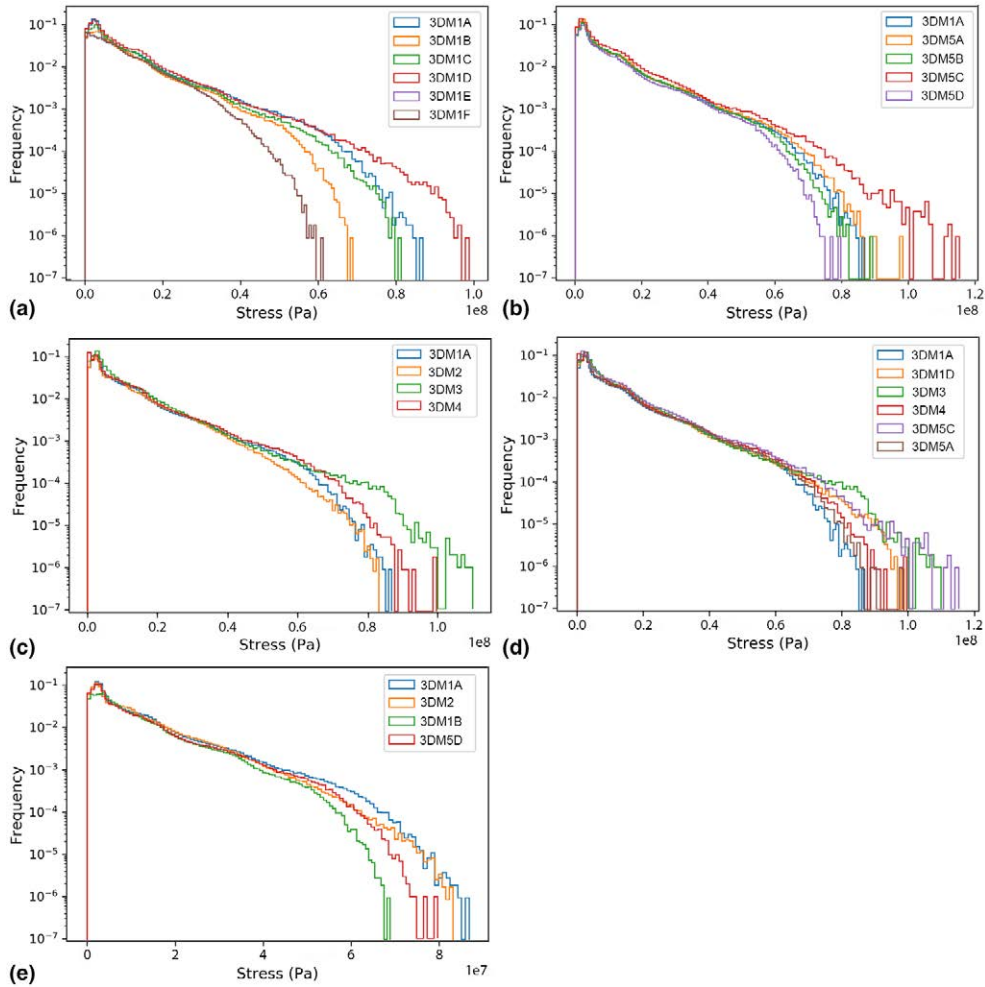
FIGURE 4 Comparison of the Von Mises stresses nodal values obtained (indicated by the frequency of each stress value interval, with the distribution of the Von Mises stresses in each model being divided into a hundred intervals) for the various 3DM1 models (a), 3DM5 models (b), 3DM2-4 models (c), and selected models with a negative (d) and a positive (e) impact, with 3DM1A as a reference. 3DM1E and 3DM1F in A have similar distributions so that only 3DM1E is visible.

that this result might be biased to some extent by the fact that, in our modelling design, stresses were applied proximally and the bone was fixed distally. However, our modelling, although realistic, shows clear simplifications, since it only includes contact compressive stresses linked to weight support and no muscular forces for example. However, this does not prevent theoretical comparisons using this simplistic modelling approach, which is the objective of this study.

3.2 | Consequences of changes in the compactness of trabecular and cortical bone

The comparison of the various 3DM1 models (Figure 2) clearly highlights a lower maximal stress in the models that are only made of a homogeneous trabecular bone, with no cortical bone (3DM1E-F; Table 1; maximal (red) values go up to 65 MPa for 3DM1E versus 85 MPa for 3DM1A from the Von Mises scales when modified in order to visualize red areas; Figures 2e and 4a). However, the outer

distribution is similar. The sections reveal that higher stress extends more internally in these models, beyond the originally cortical territory (Figure 3a,d). Interestingly, despite a change in the compactness of the trabecular bone between these two models (0.45 versus 0.55), they do not show any noticeable change in outer and inner (from the sections) stress distribution and in maximal stress values (Figures S5b,c, S9e,f; Table 1).

The 3DM1E and 3DM1F models thus show lower maximal stress than the others, with small regions where stress reaches at least 56 MPa but larger regions with stress between 28 and 37 MPa and large ones with stress higher than 18 MPa. Bone strength is correlated to its Young's modulus, with strength being assumed to be roughly one hundredth the modulus (Currey, 2006, p. 157). Compactnesses of 0.45 and 0.55 imply strengths of approximately 32 and 49 MPa, respectively, and thus lower than the maximal stress values obtained for 3DM1E-F. Conversely, compact bone's strength under compression ranges between 170 and 270 MPa in bovine bone (Currey, 2006, p. 59) and none of our models reaches von Mises stresses with such magnitude.

When cortical bone remains compact, as in 3DM1A, but that all trabecular bone is made homogeneous, we observe on the outside of the bone lower stress values for a compactness of 0.55 (3DM1B; Figure 2b), as compared to 3DM1A, although to a much lesser extent on the latero-caudal side of the diaphysis above its minimal circumference (Figure S4). This could be a consequence of a relatively higher stiffness of trabecular bone on the medial part of the bone in 3DM1A, which is thus "compensated" in 3DM1B-D by the absence of this asymmetry, and thus the lateral part being relatively stronger than in 3DM1A. Stress values increase already, as compared to 3DM1B, when compactness reaches only 0.45 (3DM1C; Figure 2c), and even more when it only reaches 0.35 (3DM1D; Figure 2d) (Figure 4a; S4b,c; S5a). This is particularly marked for the maximal stress values, as indicated by the 99th percentile values (Table 1), whereas the 95th percentile values vary poorly. The histograms reflect the higher stress values in 3DM1D compared with 3DM1A, whereas all other 3DM1 models show relatively lower values (Figure 4a). Stress on the outer bone is higher in 3DM1D than in 3DM1A except caudally where stress is lower below the humeral head (than in 3DM1A) but higher at about one third of the diaphysis caudo-laterally. This change in the distribution of the maximal stress is confirmed by the virtual sections and can justify the almost equivalent (only slightly higher in 3DM1A) 99th percentile values in these two models. However, the 95th percentile values are all below those of 3DM1A, in accordance with a distinct distribution of the stresses inside the bone, as noted from the longitudinal sections. The fact that stress in 3DM1D is lower below the humeral head than in 3DM1A is explained by the trabecular bone being particularly poorly compact in this area in 3DM1A so that it is relatively more compact and stiffer in 3DM1D.

Decreasing the compactness of the trabecular bone in the epiphyses only (3DM5A), only increases stress below the humeral head and surprisingly reduces stress between the greater tubercle and the deltoid tuberosity (Figure 5d). Conversely, when compactness is increased (3DM5B; Figure 5e), stress is slightly reduced (Figure S7b).

When the compactness of the trabecular bone changes only in the diaphysis and metaphyses, the impact on stress magnitude is higher than when it changes only in the epiphyses (Figure 5f–g; S7a,b), as also clearly indicated by the percentile values and the histograms (Table 1, Figure 4b). When compactness increases (3DM5D), stress diminishes all over the bone (with the highest values below 75 MPa; Figures 5g; S7d), and vice versa (3DM5C with highest values reaching 95 MPa; especially medially; Figure 5f).

3.3 | Influence of changes in cortical thickness

Increasing cortical thickness (3DM2) reduces maximal stress, except caudally below the humeral head up to the third of the diaphyseal length (Figure 5a). Decreasing cortical thickness (3DM3) strongly increases stress all over the bone (especially latero-caudally at the third of the diaphysis; with the highest values reaching 100 MPa; Figure 5b). The histogram shows a much stronger impact of reducing than increasing cortical thickness on the Von Mises stress values (Figure 4c). The percentile values of 3DM3 remain strangely below those of 3DM1A, which can reflect the fact that the two histograms are very close for maximal values (Figure 4c).

3.4 | Impact of a void medullary cavity

A void medullary cavity (3DM4) increases stress all over the bone (Figures 4c and 5c; Table 1). The impact is however lower than that of the reduction of cortical thickness (Figure 4c). The compactness of the trabecular bone in the diaphysis has a clear impact on stress magnitude, much more than a change in the compactness of the trabecular bone in the epiphyses (Figure 4c).

3.5 | General comparison

The microanatomical alteration that increases von Mises stresses the most is the thinning of the cortex, as this reduces the stiff surface that forces can spread upon. Next is the reduction of the compactness of the trabecular bone in the diaphysis, which has a stronger impact than the presence of a medullary cavity devoid of bone tissue (Figure 4d). Conversely, it is the reduction of the compactness in the epiphyses that causes the least changes in the von Mises stresses. The greatest reduction in the maximal stress, after the purely trabecular structures (3DM1E–F), is obtained with the homogeneous trabecular structures with the highest compactness (Figure 4e). Then it is increasing the compactness of the trabecular bone in the diaphysis and metaphyses that reduces the maximum stress the most, more than thickening the cortex (Figure 4e).

3.6 | Cumulative effects

Displaying a thicker cortex while also including a medullary cavity (Combo1), shows lower surface stresses except caudally below the humeral head up to the mid-diaphysis (Figure 6a), and higher stresses in the metaphyses (Figure 7a; S8a; S10e). Combo1 shows a global compensation of the two effects, with a rather similar histogram showing higher maximal values but less moderate ones than 3DM1A (Figure 8a).

The combination of a thinner cortex with an increased compactness of trabecular bone (Combo3), shows a change in the distribution of the Von Mises stress with a reduction of the moderate values but an increase in the maximal ones, as for Combo1, although it is not reflected in the percentile values (Table 1, Figure 8a). Stresses are generally only slightly higher than for Combo1. Stress is increased in the diaphyseal region but reduced in the metaphyses (Figure 6c; S8c; S10g). It is thus more a reorganization of the constraints associated with a different type of strengthening of the bone.

The combination of a medullary cavity with an increased compactness of trabecular bone (Combo4), shows lower stresses than
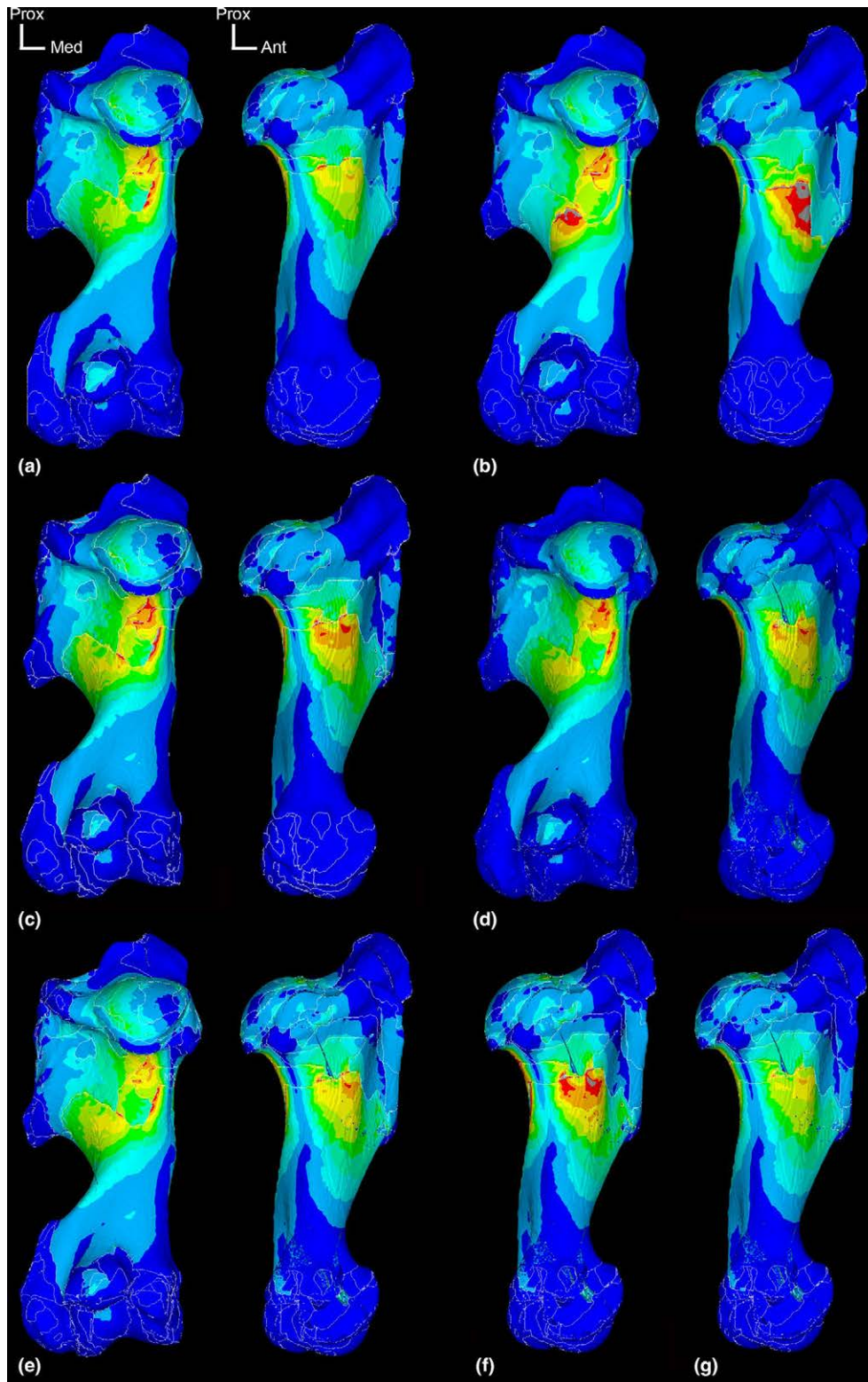
FIGURE 5 Cartographies of the Von Mises Stress distribution in (a) 3DM2 (thicker cortex), (b) 3DM3 (thinner cortex), (c) 3DM4 (open medullary cavity), (d) 3DM5A (decreased compactness in the epiphyses), (e) 3DM5B (increased compactness in the epiphyses), (f) 3DM5C (decreased compactness in the diaphysis and metaphyses), (g) 3DM5D (increased compactness in the diaphysis and metaphyses), in (from left to right) caudal and medial views, and only medial view for F and G. VM stress color scale as in Figure 2. Grey areas correspond to stress magnitudes beyond red.
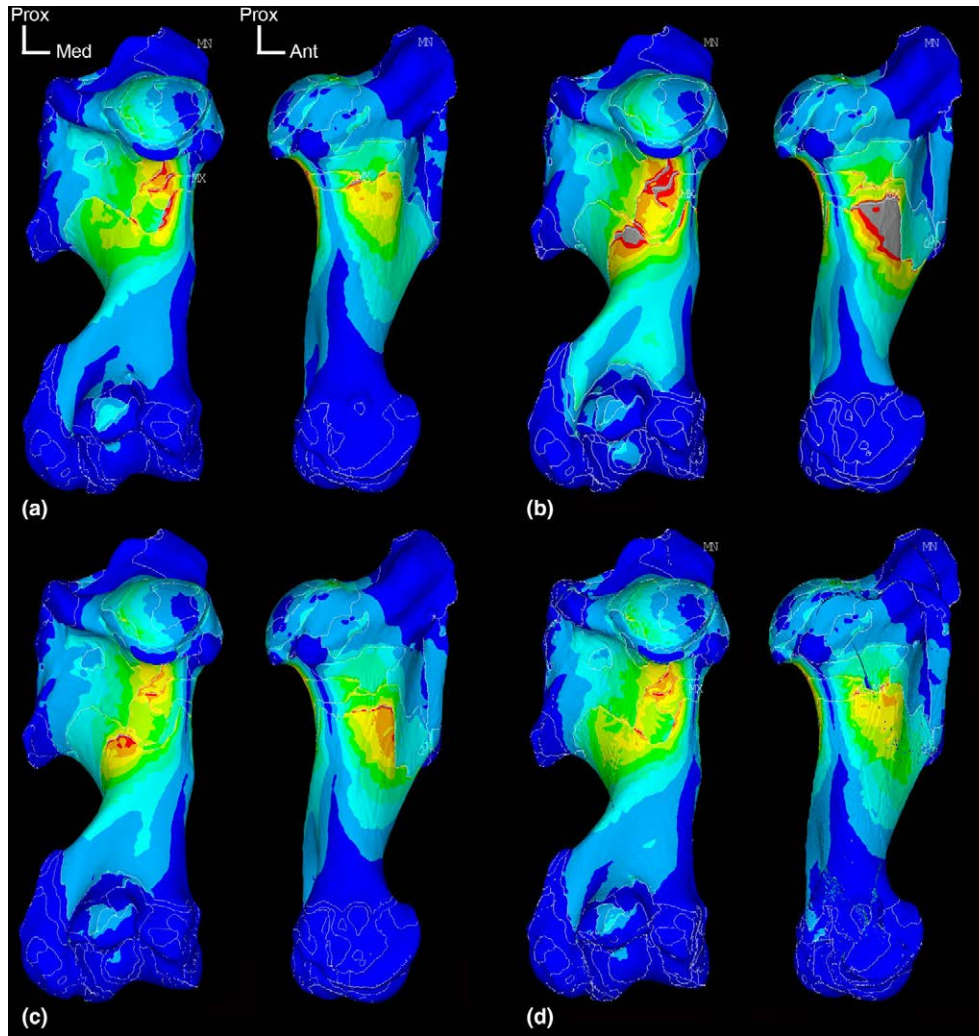
FIGURE 6 Cartographies of the Von Mises Stress distribution in (a) Combo1 (thicker cortex & open medullary cavity [MC]), (b) Combo2 (thinner cortex & MC), (c) Combo3 (thinner cortex & increased trabecular compactness [ITC]), (d) Combo4 (MC & ITC), in (from left to right) caudal and medial views. VM stress color scale (here equal for all models) as in Figure 2. Grey areas correspond to stress magnitudes beyond red.

the reference model (Figure 8a), similar stresses to 3DM1C, but higher stresses than 3DM5D (Figure 8b). The distribution of the maximal stresses on the bone surface is similar as in 3DM1A but with a general lower intensity (Figure 6d; S8d).

Cumulating a thinner cortex and a medullary cavity (Combo2) strongly weakens the bone (Figure 8a). Stress values are much higher than for 3DM1A, with maximal values up to 115 MPa, from the Von Mises scale when modified in order to visualize the highest stresses. The impact is stronger medially than laterally (Figure 6b; S8b). Longitudinal sections show that the humeral head and the metaphyses are also strongly affected (Figure 7b).

4 | DISCUSSION

Our models reveal the zones of maximum stress generated solely by the application of compressive stress, equivalent to contact load in the animal standing at rest, to the humerus of a white rhinoceros,

and how they vary in relation to changes in the inner structure of the bone. The Von Mises stress values obtained in our models are too low to generate fracture in our theoretical framework, since maximal values are always on the periphery of the cortex and rarely exceed 115 MPa (Combo2), whereas compact cortex is estimated to display a strength under compression rather close to 200 MPa (Currey, 2006, p. 59). However, as already shown on other long bones, fracture could be engendered by buckling due to compression (Houssaye et al., 2024). Moreover, as already mentioned, our biomechanical model does contain inevitable simplification regarding the loading. In particular, it only considers compression at the contact zones, but not muscle forces. Moreover, the compressive load is based on the model of a rhinoceros at rest, and could therefore naturally be much higher during locomotion. For these reasons (insufficient load magnitude and frequency), stress values were not expected to approach failure values. The aim here was not to determine whether a genuine modification to the structure of the rhinoceros humerus would lead to fracture, but to highlight and compare the impact of the different
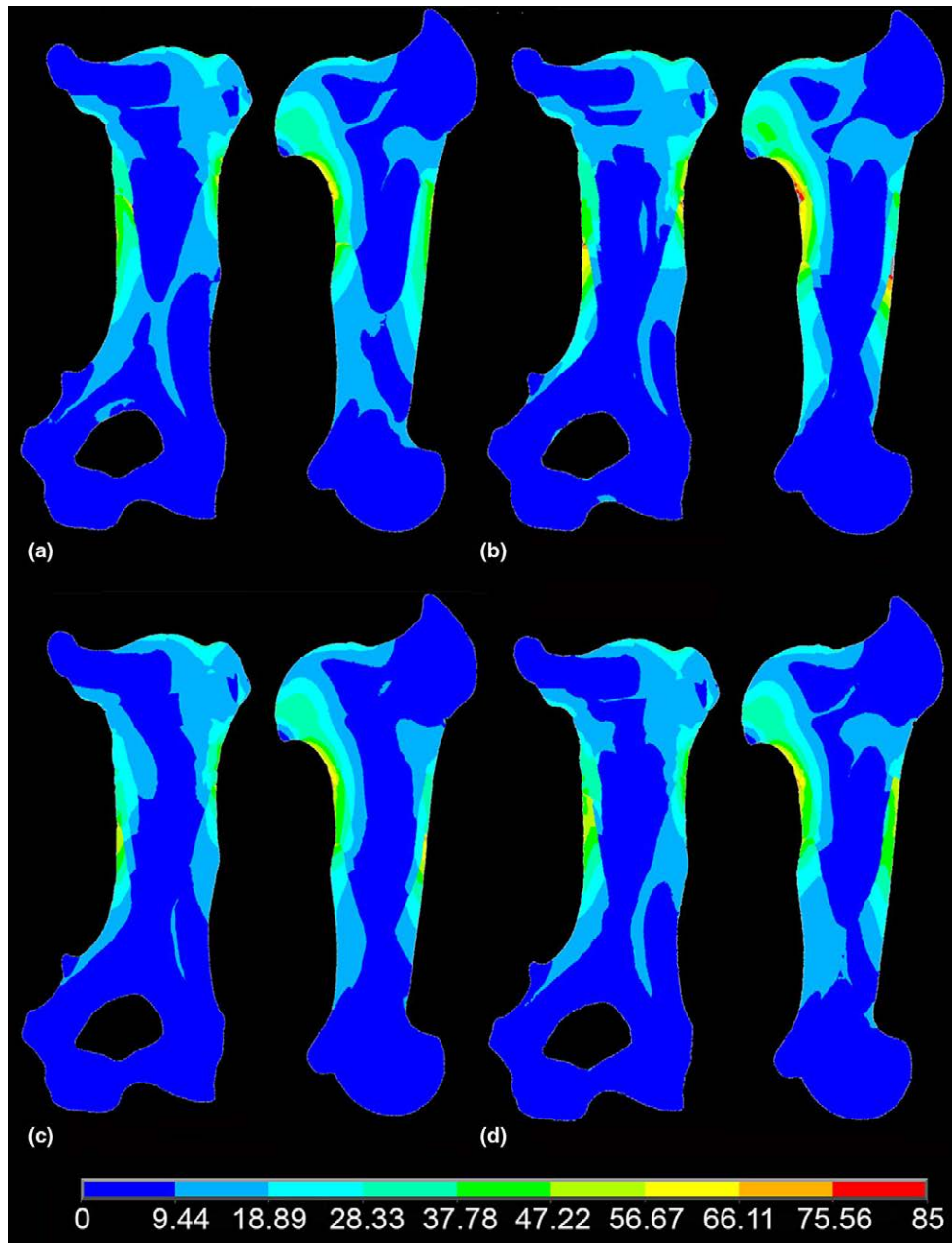
FIGURE 7 2D longitudinal sections in coronal (left) and sagittal (right) views illustrating the Von Mises stress distribution inside the bone. (a) Combo1 (thicker cortex & MC), (b) Combo2 (thinner cortex & CM), (c) Combo3 (thinner cortex & ITC), (d) Combo4 (MC & ITC). VM stress color scale in MPa.

changes in bone structure tested. Our results show that our theoretical bone models with no compact bone are more prone to failure than the reference model, even if they experience lower stress, since high stress occurs in areas of relatively low stiffness (as compared to compact cortical bone). Moreover, a lower Young's modulus also implies a lower yield stress, that is transiting from an elastic to a plastic (i.e., with irreversible deformation) behaviour, gradually weakening the bone. This underlines that the adaptation of the internal structure of the bone to resist compression is not just a matter of reducing stress in general, but of providing a resistant material where it is needed. This justifies the inner structure of the bone with a layer

of compact cortex surrounding a medullary area, with compressive stresses being transferred from the articular surfaces to the compact cortex by the osseous trabeculae. If a compact and thus stiffer structure is required to better handle muscular tensions and ensure bone movement (Currey, 2006, p. 194), it is thus also required for resisting compression.

In our *Ceratotherium* models, Von Mises stresses are negatively correlated with cortical thickness (Figure 4c). The impact of decreasing cortical thickness is much higher than that of increasing it. The cortex is in fact already proportionally much thicker in *Ceratotherium* as compared to in a smaller rhinoceros such as *Dicerorhinus* (the
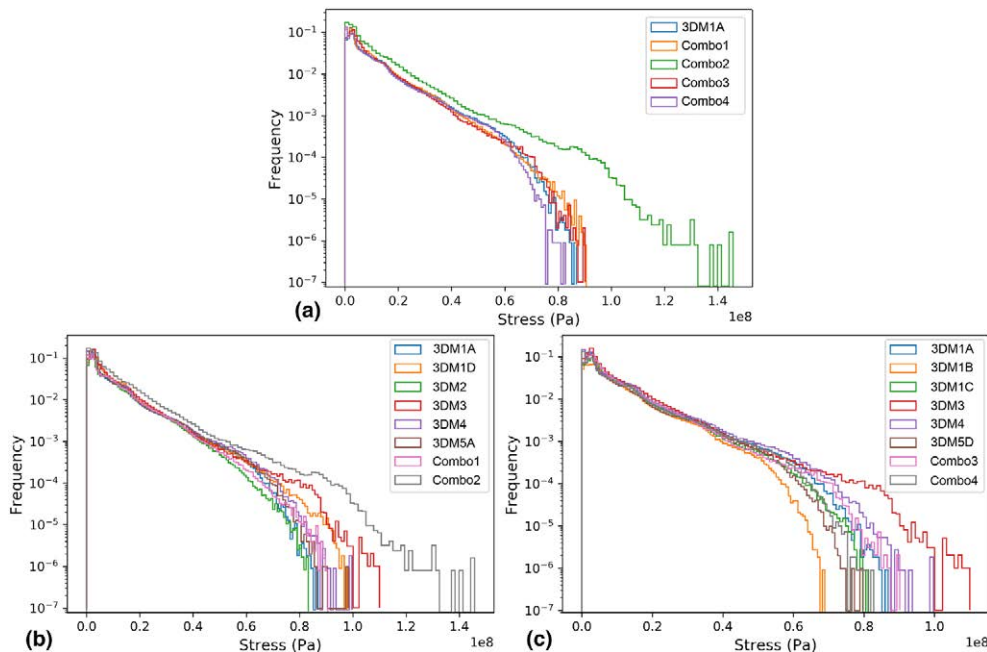
FIGURE 8 Comparison of the Von Mises stresses nodal values obtained (indicated by the frequency of each stress value interval, with the distribution of the Von Mises stresses in each model being divided into a hundred intervals) for the various Combo models (a), Combo1 and Combo2 (b) and Combo3 and Combo4 (c) with additional models for comparison, with 3DM1A as a reference.

Sumatran rhinoceros which weighs less than a ton; Dinerstein, 2011; Pers. Obs.) as in the radius and tibia of these taxa (Houssaye et al., 2024). The strong impact of reducing cortical thickness on maximal stress values highlights the essential role of the thick cortex of *Ceratotherium* humerus to help resist compressive forces, as previously suggested, but never tested, in microanatomical studies of large mammals (Houssaye et al., 2016c, 2021). However, our study has revealed that the most efficient way of reducing stresses is not cortical thickening but an increase in the compactness of the trabecular bone, especially in the diaphysis and metaphyses. Accordingly, the occurrence of an open medullary cavity increases the stresses, which confirms previous hypotheses that the filling of the medullary with trabecular bone in heavy taxa was beneficial in resisting compression (Carter & Beaupré, 2000; Oxnard, 1993). However, our results more surprisingly reveal that the medullary cavity in itself has less impact than diminishing trabecular compactness in the diaphysis and metaphyses (on the highest values especially), which is nevertheless consistent with constraints being minimal in the core of a cylinder under compression and associated bending (Currey, 2006, p. 199). Changes in epiphyseal compactness have a limited impact compared with other microanatomical modifications. This may reflect the rather limited impact of a change in compactness for contact forces in these areas and rather a link between their trabecular compactness and the stresses associated with muscle insertions, muscular insertions being indeed more numerous on the epiphyses, with, on average, stronger muscles (Etienne et al., 2024).

The models combining two features with expected opposite effects combine for one the features with the strongest impacts (Combo3: cortical thinning and higher trabecular compactness), and for the other features with more moderate impacts (Combo2: occurrence of a medullary cavity and cortical thickening). Both show a rather neutral result with a different distribution of the stresses inside the bone but not so strong differences in the general stress values. These different strategies can be observed in various taxa in which compression is assumed to be rather high in association with their heavy weight, such as a thin cortex but a complete filling of the medullary area by a spongiosa in the sauropod dinosaur *Nigersaurus* (Lefebvre et al., 2023) versus a thicker cortex and an open medullary cavity in the largest bovids (Pers. obs.) and cervids (Houssaye et al., 2021). The combination of an increased trabecular bone compactness with a medullary cavity, and thus of a factor with a potentially high positive impact and one with a moderate negative impact, shows a positive cumulative impact. The model combining two features with an expected negative impact shows a much higher increase in stress intensity than the sum of the two features taken in isolation, as clearly shown on the histogram (the area between Combo2 and 3DM1A being much larger than the sum of the areas between 3DM1A and 3DM3 and 3DM4, respectively; Figure 8b).

Only a few biomechanical studies dealing with evolutionary biology questions take bone inner structure into account. Instead, they generally consider bones as homogeneous (e.g., Coatham et al., 2020; Cox et al., 2011; Goussard et al., 2010; Lautenschlager et al., 2018; O'Higgins et al., 2011; Snively et al., 2015). Conversely, the heterogeneous structure of the bones is considered, and even the focus of certain biomechanical studies, in bone biology. This is done either on complete bones, notably on the basis of bone density or general inner architecture, or on regions of interest, this time with more detailed structures (with individualized trabeculae)

(Christen et al., 2014; Gröning et al., 2012; Helgason et al., 2008; Kainz et al., 2020; Morgan & Bouxsein, 2005; Querol et al., 2006; Rudman et al., 2006). Thanks in particular to the development of microtomography and computing capacities that have made it possible to process very large quantities of data in biomechanical analyses, some recent morpho-functional studies in evolutionary biology have incorporated the heterogeneous inner structure of bones in their analyses on partial bones or even, more rarely, on complete ones (Mielke & Nyakatura, 2019; Van Leeuwen et al., 2022; Clarac et al., 2024). Our study highlights the relative impact of microanatomical features on bone biomechanics. It would be interesting to estimate the relative impact generated by different heterogeneous inner structures versus a homogeneous one for a single bone in analyses comparing the biomechanical properties (e.g., bone strength, load distribution under specific loads…) of several bones.

This study focused on bone strength under compression. It allowed us to isolate various microanatomy-strength under compression relationships through modeling and to compare their relative intensities, as well as the result of the co-occurrence of pairs of these relationships. This test of isolated form-function relationships, which are otherwise mixed in nature, and their comparison serves to better understand bone adaptation. This can be of great use to improve paleobiological and archeozoological inferences from the study of fossil bones. Here only bone compactness was modified, in various parts of a reference bone model. To date, the full bone's structure with individualized trabeculae cannot be incorporated into ANSYS, at least not for a rhinoceros. Until computer developments make this possible, it would be interesting to continue looking at other form-function relationships through simplified modeling. We could isolate the impact of similar microanatomical features this time under stress generated by muscular activities, or focus on the impact of anisotropy, using various grids. Moreover, similar modeling approaches with one-by-one parameter changes can be used to perform various sensitivity analyses, in order to estimate the relative impact of simplifications or choices in biomechanical models (for example, in relation to the areas where the bone is constrained and the force applied, to the different grids used as compared to the original trabecular network, or to modeling parameters such as the number of faces), but this time with models as close as possible to true biology.

In addition, our results have potential relevance for bioinspiration. Indeed, this design approach, which uses observations of biological systems to design innovative structures (Adriaens, 2019), requires the isolation of single form-function relationships from biological sources. Bone is now increasingly used for bioinspiration in various fields (see details and references in Houssaye et al., 2024) and determining clear form-function relationships in bone structure offers great potential for bioinspiration.

5 | CONCLUSION

This innovative modelling enabled us to highlight the relative impact of various bone microanatomical parameters on the magnitude and distribution of Von Mises stresses in the humerus of a white rhinoceros under compression. Our study confirmed previous hypotheses about the role of a thickening of the cortex and the filling of the medullary area by trabecular bone to better resist high compression in heavy taxa, with however a stronger impact of increasing trabecular bone compactness than of avoiding an open medullary cavity. These analyses have also highlighted the lower impact of the compactness of the trabecular bone in the epiphyses, as compared to in the diaphysis, for resisting compressive forces. Moreover, it has shown that if microanatomical changes of opposite but of similar amplitude impact can compensate each other, the impact of the sum of two negative microanatomical changes far exceeds the sum of the impacts of each of the two changes taken separately. Such conclusions enable us to validate and better estimate previous form-function relationships and to allow them to be used for paleobiological and archeozoological inferences. These form-function biomechanical rules can also be used for bioinspiration to build more resistant structures with less material. The bone biomechanical relationships highlighted in this study could thus be used in various "weight support" structures. Further studies with such a modelling approach, focusing on muscular constraints or on other bone parameters for example, could provide additional form-function relationships to better characterize bone adaptation. Our study also highlights the significant impact of the inner structure on the results of FE analyses, and thus the interest to take it into account in biomechanical studies. Further modelling studies, this time on several bones and on models closer to biological conditions, could help to better estimate its relative impact in comparative studies.

DATA AVAILABILITY STATEMENT
The scan of the bone analysed in this study is available upon request from MNHN's 3Dthèque (https://3dtheque.mnhn.fr/work?platform=astrx).

ORCID
Cyril Etienne https://orcid.org/0000-0002-4548-2934
Alexandra Houssaye https://orcid.org/0000-0001-8789-5545

REFERENCES
Adriaens, D. (2019) Evomimetics: the biomimetic design thinking 2.0. In: *Bioinspiration, biomimetics, and bioreplication IX*. Bellingham, WA: SPIE, pp. 41–53.

Arganda-Carreras, I., Kaynig, V., Rueden, C., Eliceiri, K.W., Schindelin, J., Cardona, A. et al. (2017) Trainable Weka segmentation: a machine learning tool for microscopy pixel classification. *Bioinformatics*, 33, 2424–2426.

Canoville, A., De Buffrénil, V. & Laurin, M. (2021) Bone microanatomy and lifestyle in tetrapods. In: de Buffrénil, V., de Ricqlès, A.J., Zylberberg, L. & Padian, K. (Eds.) *Vertebrate skeletal histology and Paleohistology*. Boca Raton & London: CRC Press, pp. 724–743.

Canoville, A. & Laurin, M. (2010) Evolution of humeral microanatomy and lifestyle in amniotes, and some comments on palaeobiological inferences. *Biological Journal of the Linnean Society*, 100, 384–406.

Carter, D.R. & Beaupré, G.S. (2000) *Skeletal function and form: Mechanobiology of skeletal development, aging, and regeneration*. Cambridge: Cambridge University Press.

Castelló, J.R. (2016) *Bovids of the world*. Princeton & Oxford: Princeton University Press.

Cerda, I.A., García, R.A., Powell, J.E. & Lopez, O. (2015) Morphology, microanatomy, and histology of titanosaur (Dinosauria, Sauropoda) osteoderms from the upper cretaceous of Patagonia. *Journal of Vertebrate Paleontology*, 35, e905791.

Christen, P., Ito, K., Ellouz, R., Boutroy, S., Sornay-Rendu, E., Chapurlat, R.D. et al. (2014) Bone remodelling in humans is load-driven but not lazy. *Nature Communications*, 5, 4855.

Clarac, F., Cornille, A., Bijl, S. & Sanchez, S. (2024) Tetrapod terrestrialisation: a weight-bearing potential already present in the humerus of the stem-tetrapod fish *Eusthenopteron* foordi. *bioRxiv*, 2024-02.

Coatham, S.J., Vinther, J., Rayfield, E.J. & Klug, C. (2020) Was the Devonian placoderm *Titanichthys* a suspension feeder? *Royal Society Open Science*, 7, 200272.

Cox, P.G., Fagan, M.J., Rayfield, E.J. & Jeffery, N. (2011) Finite element modelling of squirrel, Guinea pig and rat skulls: using geometric morphometrics to assess sensitivity. *Journal of Anatomy*, 219, 696–709.

Currey, J.D. (2006) *Bones: structure and mechanics*. Princeton & Woodstock: Princeton university press.

DeMars, L.J., Stephens, N.B., Saers, J.P., Gordon, A., Stock, J.T. & Ryan, T.M. (2021) Using point clouds to investigate the relationship between trabecular bone phenotype and behavior: an example utilizing the human calcaneus. *American Journal of Human Biology*, 33, e23468.

Dinerstein, E. (2011) Family Rhinocerotidae (Rhinoceroses). In: Wilson, D.E. & Mittermeier, R.A. (Eds.) *Handbook of the mammals of the world*. Barcelona: Lynx Edicions, pp. 144–181.

Dumont, M., Laurin, M., Jacques, F., Pellé, E., Dabin, W. & de Buffrénil, V. (2013) Inner architecture of vertebral centra in terrestrial and aquatic mammals: a two-dimensional comparative study. *Journal of Morphology*, 274, 570–584.

Dunmore, C.J., Bardo, A., Skinner, M.M. & Kivell, T.L. (2020) Trabecular variation in the first metacarpal and manipulation in hominids. *American Journal of Physical Anthropology*, 171, 219–241.

Dutto, D.J., Hoyt, D.F., Clayton, H.M., Cogger, E.A. & Wickler, S.J. (2006) Joint work and power for both the forelimb and hindlimb during trotting in the horse. *Journal of Experimental Biology*, 209, 3990–3999.

Etienne, C., Houssaye, A., Fagan, M.J. & Hutchinson, J.R. (2024) Estimation of the forces exerted on the limb long bones of a white rhinoceros (*Ceratotherium simum*) using musculoskeletal modelling and simulation. *Journal of Anatomy*, 245, 240–257.

Gould, S.J. (2006) *The structure of evolutionary theory*. Harvard University Press.

Goussard, F., Germain, D., Delmer, C. & Moreno, K. (2010) Finite element analysis: a promising tool for the reconstruction of extinct vertebrate graviportal taxa. A preliminary study based on the metacarpal arrangement of Elephas maximus. *Comptes Rendus Palevol*, 9, 455–461.

Gröning, F., Fagan, M. & O'higgins, P. (2012) Modeling the human mandible under masticatory loads: which input variables are important? *The Anatomical Record: Advances in Integrative Anatomy and Evolutionary Biology*, 295, 853–863.

Hayashi, S., Houssaye, A., Nakajima, Y., Chiba, K., Ando, T., Sawamura, H. et al. (2013) Bone inner structure suggests increasing aquatic adaptations in Desmostylia (Mammalia, Afrotheria). *PLoS One*, 8, e59146.

Helgason, B., Taddei, F., Pálsson, H., Schileo, E., Cristofolini, L., Viceconti, M. et al. (2008) A modified method for assigning material properties to FE models of bones. *Medical Engineering & Physics*, 30, 444–453.

Houssaye, A., Etienne, C., Gallic, Y., Rocchia, F. & Chaves-Jacob, J. (2024) How can research on modern and fossil bones help us build more resistant columns? *Bioinspiration & Biomimetics*, 19, 36007.

Houssaye, A., Fernandez, V. & Billet, G. (2016) Hyperspecialization in some south American endemic ungulates revealed by long bone microstructure. *Journal of Mammalian Evolution*, 23, 221–235.

Houssaye, A., Martin, F., Boisserie, J.-R. & Lihoreau, F. (2021) Paleoecological inferences from long bone microanatomical specializations in Hippopotamoidea (Mammalia, Artiodactyla). *Journal of Mammalian Evolution*, 28, 847–870.

Houssaye, A., Martin Sander, P. & Klein, N. (2016) Adaptive patterns in aquatic amniote bone microanatomy—more complex than previously thought. *Integrative and Comparative Biology*, 56, 1349–1369.

Houssaye, A., Taverne, M. & Cornette, R. (2018) 3D quantitative comparative analysis of long bone diaphysis variations in microanatomy and cross-sectional geometry. *Journal of Anatomy*, 232, 836–849.

Houssaye, A., Waskow, K., Hayashi, S., Cornette, R., Lee, A.H. & Hutchinson, J.R. (2016) Biomechanical evolution of solid bones in large animals: a microanatomical investigation. *Biological Journal of the Linnean Society*, 117, 350–371.

Kainz, H., Killen, B.A., Wesseling, M., Perez-Boerema, F., Pitto, L., Garcia Aznar, J.M. et al. (2020) A multi-scale modelling framework combining musculoskeletal rigid-body simulations with adaptive finite element analyses, to evaluate the impact of femoral geometry on hip joint contact forces and femoral bone growth. *PLoS One*, 15, e0235966.

Kivell, T.L., Skinner, M.M., Lazenby, R. & Hublin, J. (2011) Methodological considerations for analyzing trabecular architecture: an example from the primate hand. *Journal of Anatomy*, 218, 209–225.

Klein, N., Canoville, A. & Houssaye, A. (2019) Microstructure of vertebrae, ribs, and gastralia of Triassic sauropterygians—new insights into the microanatomical processes involved in aquatic adaptations of marine reptiles. *The Anatomical Record*, 302, 1770–1791.

Ksepka, D.T., Werning, S., Sclafani, M. & Boles, Z.M. (2015) Bone histology in extant and fossil penguins (Aves: Sphenisciformes). *Journal of Anatomy*, 227, 611–630.

Laasanen, M., Töyräs, J., Korhonen, R., Rieppo, J., Saarakkala, S., Nieminen, M. et al. (2003) Biomechanical properties of knee articular cartilage. *Biorheology*, 40, 133–140.

Lautenschlager, S., Gill, P.G., Luo, Z.X., Fagan, M.J. & Rayfield, E.J. (2018) The role of miniaturization in the evolution of the mammalian jaw and middle ear. *Nature*, 561, 533–537.

Lefebvre, R., Allain, R. & Houssaye, A. (2023) What's inside a sauropod limb? First three-dimensional investigation of the limb long bone microanatomy of a sauropod dinosaur, *Nigersaurus taqueti* (Neosauropoda, Rebbachisauridae), and implications for the weight-bearing function. *Palaeontology*, 66, e12670.

Lessertisseur, J. & Saban, R. (1967) Squelette appendiculaire. In: Grassé, P.-P. (Ed.) *Traité de zoologie anatomie, systématique, biologie - Mammifères téguments, squelette (Tome XVI, fascicule 1)*. Paris: Masson, pp. 709–1078.

Mallet, C., Cornette, R., Billet, G. & Houssaye, A. (2019) Interspecific variation in the limb long bones among modern rhinoceroses—extent and drivers. *PeerJ*, 7, e7647.

Mancini, I., Rieppo, L., Pouran, B., Afara, I., Braganca, F.S., van Rijen, M. et al. (2019) Effects of body mass on microstructural features of the osteochondral unit: a comparative analysis of 37 mammalian species. *Bone*, 127, 664–673.

Maquer, G., Musy, S.N., Wandel, J., Gross, T. & Zysset, P.K. (2015) Bone volume fraction and fabric anisotropy are better determinants of trabecular bone stiffness than other morphological variables. *Journal of Bone and Mineral Research*, 30, 1000–1008.

Mielke, M. & Nyakatura, J.A. (2019) Bone microstructure in finite element modeling: the functional role of trabeculae in the femoral head of Sciurus vulgaris. *Zoomorphology*, 138, 535–547.

Mielke, M., Wölfer, J., Arnold, P., van Heteren, A.H., Amson, E. & Nyakatura, J.A. (2018) Trabecular architecture in the sciuromorph femoral head: allometry and functional adaptation. *Zoological Letters*, 4, 1–11.

Morgan, E.F. & Bouxsein, M.L. (2005) Use of finite element analysis to assess bone strength. *BoneKEy-Osteovision*, 2, 8–19.

Nganvongpanit, K., Siengdee, P., Buddhachat, K., Brown, J.L., Klinhom, S., Pitakarnnop, T. et al. (2017) Anatomy, histology and elemental profile of long bones and ribs of the Asian elephant (*Elephas maximus*). *Anatomical Science International*, 92, 554–568.

O'Higgins, P., Cobb, S.N., Fitton, L.C., Gröning, F., Phillips, R., Liu, J. et al. (2011) Combining geometric morphometrics and functional simulation: an emerging toolkit for virtual functional analyses. *Journal of Anatomy*, 218, 3–15.

Oxnard, C.E. (1993) Bone and bones, architecture and stress, fossils and osteoporosis. *Journal of Biomechanics*, 26, 63–79.

Quemeneur, S., De Buffrenil, V. & Laurin, M. (2013) Microanatomy of the amniote femur and inference of lifestyle in limbed vertebrates. *Biological Journal of the Linnean Society*, 109, 644–655.

Querol, L.B., Büchler, P., Rueckert, D., Nolte, L.P. & Ballester, M.Á.G. (2006) Statistical finite element model for bone shape and biomechanical properties. In: *Medical image computing and computer-assisted intervention–MICCAI 2006: 9th international conference, Copenhagen, Denmark, October 1–6, 2006. Proceedings, part I 9.* Berlin Heidelberg: Springer, pp. 405–411.

Rayfield, E.J. (2007) Finite element analysis and understanding the biomechanics and evolution of living and fossil organisms. *Annual Review of Earth and Planetary Sciences*, 35, 541–576.

Ren, L., Miller, C.E., Lair, R. & Hutchinson, J.R. (2010) Integration of biomechanical compliance, leverage, and power in elephant limbs. *Proceedings of the National Academy of Sciences*, 107, 7078–7082.

Rudman, K.E., Aspden, R.M. & Meakin, J.R. (2006) Compression or tension? The stress distribution in the proximal femur. *Biomedical Engineering Online*, 5, 1–7.

Saers, J.P., Cazorla-Bak, Y., Shaw, C.N., Stock, J.T. & Ryan, T.M. (2016) Trabecular bone structural variation throughout the human lower limb. *Journal of Human Evolution*, 97, 97–108.

Schindelin, J., Arganda-Carreras, I., Frise, E., Kaynig, V., Longair, M., Pietzsch, T. et al. (2012) Fiji: an open-source platform for biological-image analysis. *Nature Methods*, 9, 676–682.

Seilacher, A. (1970) Arbeitskonzept zur konstruktions-morphologie. *Lethaia*, 3, 393–396.

Snively, E., Fahlke, J.M. & Welsh, R.C. (2015) Bone-breaking bite force of *Basilosaurus isis* (Mammalia, Cetacea) from the late Eocene of Egypt estimated by finite element analysis. *PLoS One*, 10(2), e0118380.

Stauber, M., Rapillard, L., van Lenthe, G.H., Zysset, P. & Müller, R. (2006) Importance of individual rods and plates in the assessment of bone quality and their contribution to bone stiffness. *Journal of Bone and Mineral Research*, 21, 586–595.

Straehl, F.R., Scheyer, T.M., Forasiepi, A.M., MacPhee, R.D. & Sanchez-Villagra, M.R. (2013) Evolutionary patterns of bone histology and bone compactness in xenarthran mammal long bones. *PLoS One*, 8, e69275.

Turner, C.H. (1998) Three rules for bone adaptation to mechanical stimuli. *Bone*, 23, 399–407.

Van Leeuwen, T., Schneider, M.T., van Lenthe, G.H. & Vereecke, E.E. (2022) The effect of different grasping types on strain distributions in the trapezium of bonobos (*pan paniscus*). *Journal of Biomechanics*, 144, 111284.

Wall, W.P. (1983) The correlation between high limb-bone density and aquatic habits in recent mammals. *Journal of Paleontology*, 57, 197–207.

Walmsley, C.W., McCurry, M.R., Clausen, P.D. & McHenry, C.R. (2013) Beware the black box: investigating the sensitivity of FEA simulations to modelling factors in comparative biomechanics. *PeerJ*, 1, e204.

SUPPORTING INFORMATION

Additional supporting information can be found online in the Supporting Information section at the end of this article.